BNL-229391-2026-JAAM

Spatiotemporal and Statistical Mapping of Transition Metal Equilibria in Alkaline Media

A. Promi, Y. Yang

To be published in "Chemistry of Materials"

February 2026

Photon Sciences

Brookhaven National Laboratory

U.S. Department of Energy

USDOE Office of Science (SC), Basic Energy Sciences (BES). Scientific User Facilities (SUF)

DISCLAIMER

Spatiotemporal and Statistical Mapping of Transition Metal Equilibria in Alkaline Media

Anika Tabassum Promi[1], Jaeyoung Lee[2], Katelyn Meyer[1,3], Dawei Xia[1], Chenguang Shi[1], Yang Yang[4], Andrew M. Kiss[4], Luxi Li[5], Chengjun Sun[5], Dennis Nordlund[6], F. Marc Michel[7], Hongxiao Zhu[2] and Feng Lin[1,3]*

[1] *Department of Chemistry, Virginia Tech, Blacksburg, Virginia 24061, United States*

[2] *Department of Statistics, Virginia Tech, Blacksburg, Virginia 24061, United States*

[3] *School of Engineering, Brown University, Providence, Rhode Island 02912, United States*

[4] *National Synchrotron Light Source II, Brookhaven National Laboratory, Upton, NY, 11973, United States*

[5] *X-Ray Science Division, Argonne National Laboratory, Lemont, IL, 60439, United States*

[6] *Stanford Synchrotron Radiation Lightsource, SLAC National Accelerator Laboratory, Menlo Park, California 94025, United States*

[7] *Department of Geosciences, Virginia Tech, Blacksburg, Virginia 24061, United States*

* Corresponding author: feng_lin@brown.edu

Abstract

Transition metal dissolution and redeposition (D/R) kinetics in alkaline media play a critical role in various chemical and electrochemical processes. Competitive reaction kinetics between different transition metals can modulate individual metal behavior in these processes. To date, these phenomena have remained largely unmeasured, and even when captured, they are difficult to statistically characterize due to their dynamic nature, simultaneous occurrence, and spatially heterogeneous nature. Here, we develop a statistical analysis framework based on in-situ and operando X-ray fluorescence microscopy (XFM) to investigate the relative D/R kinetics of multiple transition metals in alkaline media. By employing statistical analysis, we quantify the spatial distribution of D/R species and assess the rate at which the system reaches equilibrium under varying reaction conditions. We show that pH does not simply change the rate of dissolution and redeposition, but reorganizes the cross-element kinetic correlations among Ni, Fe, and Mn and accelerates the spatial equilibration of D/R events, as quantified through correlation analysis, reaction-rate estimation, probability function distributions, and texture-based monitoring statistics. . Additionally, we demonstrate how modifying the solvent environment can influence D/R kinetics, providing a pathway for tuning materials synthesis and process optimization. Our study offers valuable insights into the complex interplay between different transition metals and provides a reliable statistical framework for spatial analysis of diverse imaging datasets, enabling deeper extraction of latent information across multiple modalities.

Introduction

The solid-liquid interfacial dissolution and simultaneous redeposition of transition metals in alkaline media govern reaction kinetics across diverse systems, influencing how materials evolve, react and stabilize over time. The ubiquity of these dissolution/redeposition (D/R) mechanisms spans geological mineral evolution[1] to modern electrochemical systems, where they critically determine performance metrics in applications ranging from batteries to electrocatalysts.[2–10] For example, archaeological studies of Roman glass artifacts show that millennia of alkaline weathering drive silica dissolution, followed by nanoparticle reprecipitation. Over time, these nanoparticles self-assemble into ordered photonic crystals, with the process modulated by pH cycles.[1] Similar interfacial dynamics govern modern electrochemical systems, but on much faster timescales due to elevated temperatures, applied potentials, or reactive environments. For example, in aqueous zinc-manganese oxide batteries, transition metal D/R are crucial for the charge storage mechanism, facilitating reversible solid-aqueous phase transformations that enable efficient battery operation.[11] In electrocatalysis, electrical potential-dependent transition metal D/R has been found to cause catalyst surface reconstruction and deactivation.[3–5] Figure 1a highlights several key applications that can benefit from a deeper understanding of transition metal D/R in alkaline media, including battery degradation, catalyst stability, metal recovery, and nanomaterial synthesis. These examples underscore the critical balance required in harnessing the D/R phenomena, whether leveraging it for materials engineering or mitigating its degradation pathways.

Understanding D/R processes can be particularly challenging in complex multicomponent systems where multiple transition metals coexist and interact. Unlike single-metal systems where kinetics can often be studied in isolation, multimetal environments show interdependent D/R behavior influenced by solubility limits, ligand binding strength, pH-dependent supersaturation, and local redox reactions. In such systems, one metal may exhibit delayed redeposition due to stable complex formation, while another may undergo nearly instantaneous redeposition due to extremely low solubility. In some cases, metals may undergo repeated redox cycles that add

variability to the spatial and temporal characteristics of D/R behavior, further complicating system dynamics. Furthermore, individual metals may respond differently to changes in pH, complicating the identification of conditions that support balanced D/R behavior across the entire system. These behaviors can also vary spatially due to localized differences in reaction rates, equilibration times, and metal interactions, often leading to spatial heterogeneity. Traditional characterization methods lack the resolution to disentangle these overlapping dynamic behaviors, particularly when trying to identify what drives asynchronous reactions or the spatial co-localization of metals. Addressing these challenges requires not only element-specific detection, but also spatiotemporal quantification of how D/R patterns evolve under varying reaction conditions.

To unravel these complexities, we turn to in-situ synchrotron-based X-ray fluorescence microscopy (XFM), which provides two-dimensional, element-specific maps with strong penetration depth, enabling us to track metal distributions across the sample volume. XFM allows us to visualize and quantify subtle changes in both dissolution and redeposition, making it a uniquely powerful tool for studying D/R phenomena in multimetal systems. Prior work using in-situ XFM has studied voltage-dependent Mn redistribution in battery cathodes and phase segregation in electrolytes and electrocatalysts, demonstrating its utility in resolving coupled chemical and spatial dynamics.[3,12–15] To advance this capability, we integrate XFM with statistical analysis to extract quantitative insights into reaction rates, spatial distributions, and metal–metal correlations during dynamic D/R processes.

Using a model $Ni_{1/3}Fe_{1/3}Mn_{1/3}(OH)_{2+x}$ material with equimolar metal content, we systematically vary pH and solvent composition to isolate intrinsic interfacial reactivity. Our findings reveal that each metal exhibits distinct pH-dependent D/R coupling. Higher alkalinity accelerates spatial equilibration and promotes more uniform spatial D/R distributions. Targeted ion additions allow selective tuning of reaction rates based on the chemical environment. Together, these insights establish a framework for decoding and controlling multimetal D/R processes in alkaline systems, with broad relevance to batteries, electrocatalysts, and nanomaterial synthesis.

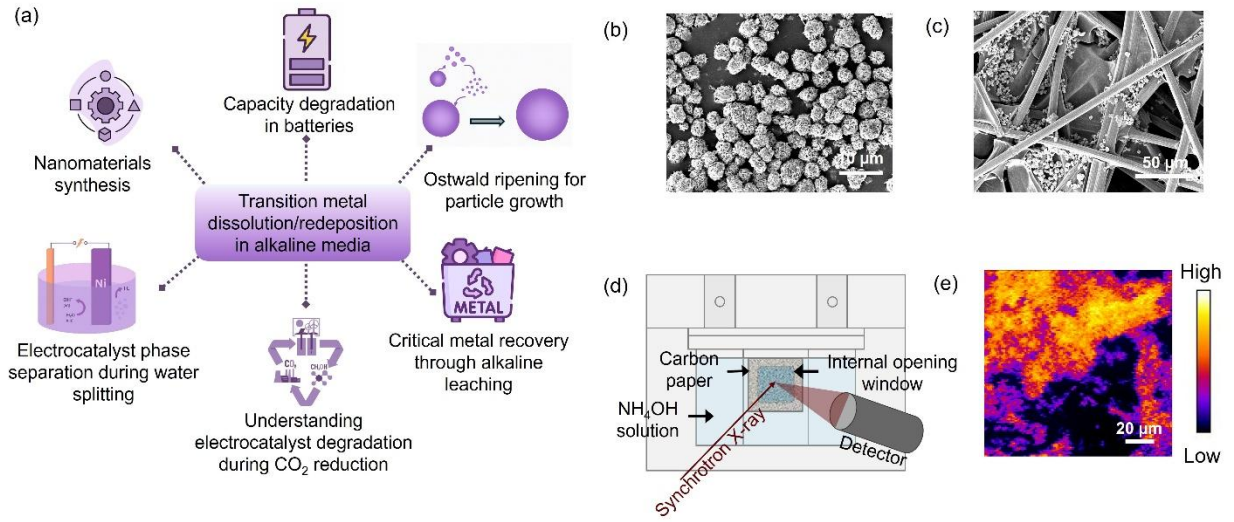

Figure 1: (a) Schematic illustration of transition metal dissolution/redeposition phenomena governing numerous chemical, electrochemical and synthetic processes; (b) Morphology of the $Ni_{1/3}Fe_{1/3}Mn_{1/3}(OH)_{2+x}$ particles used to study the simultaneous D/R behavior of Ni, Fe and Mn ions in NH_4OH, captured with scanning electronic microscopy (SEM); (c) SEM image of the $Ni_{1/3}Fe_{1/3}Mn_{1/3}(OH)_{2+x}$ particles deposited on the carbon paper; (d) schematic illustration of the specially designed cell for the in-situ XFM experiments at the 5-ID-SRX beamline at the National Synchrotron Light Source II;[16] (e) Example of an in-situ XFM mapping of the sample which was collected after immersing the sample in NH_4OH in the in-situ cell, where the color code denotes the relative transition metal concentration. The image is composed of 140×140 pixels with each pixel corresponding to 1 µm area on the sample. This image shows relative Ni distribution throughout the sample when the pH of the NH_4OH was 10.5. Areas with high intensity correspond to higher concentration of Ni and areas with lower intensity correspond to lower concentration of Ni.

Materials Characterization and Experimental Setup

We selected $Ni_{1/3}Fe_{1/3}Mn_{1/3}(OH)_{2+x}$ with a hexagonal crystal structure (Figure S1) and plate-like aggregated morphology as the model system (Figure 1b and Figure S2). Elemental and spectroscopic analysis confirmed equimolar metal distribution (Table S1) and revealed Ni^{2+}, Fe^{3+}, and mixed Mn oxidation states at both surface and bulk levels (Figures S3–S4).

The $Ni_{1/3}Fe_{1/3}Mn_{1/3}(OH)_{2+x}$ material was drop cast onto a Toray carbon paper (hereafter referred to as the 'substrate'), which was then attached to a custom-designed cell. SEM image of the substate is shown in Figure 1c, which shows that the particles are well dispersed within the carbon fibers. The substrate was then immersed in ammonium hydroxide solutions of varying pH

(10.5, 11.0, and 11.5). This setup was used for in-situ synchrotron X-ray fluorescence microscopy (XFM) measurements, which tracked the fluorescence intensity of Ni, Fe, and Mn simultaneously on the substrate as a function of time. Schematic illustration of the cell setup is shown in Figure 1d. Figure 1e presents a representative Ni distribution map acquired over a 13-minute scan while the sample remained immersed in NH_4OH solution at pH 10.5. Pixel-wise image subtraction was used to extract net dissolution and redeposition events, forming the basis of our spatial and temporal analysis of D/R behavior across metals and pH conditions. Details of material synthesis, cell design, substrate preparation, data acquisition and data analysis method are provided in the Supplementary Information (Figure S5-S8).

Image Classification into 'Dissolution' and 'Redeposition' Datasets

To quantify spatially resolved dissolution and redeposition events, a time-resolved image subtraction approach was implemented using Python. First, the images in the datasets were stabilized against sample movement and drifting using ImageJ. Then a 2 × 2 pixel binning was used to improve the accuracy of the spatial analysis. Then using these binned images, the pixel-wise difference was computed for each pair of consecutive images. Positive values, corresponding to increased signal intensity, were isolated to represent net redeposition, while negative values, corresponding to decreased intensity, were isolated to represent net dissolution. These two components were saved as separate grayscale images, generating time series datasets that reflect the spatial and temporal evolution of redeposition and dissolution processes, respectively. The process is shown in images in Figure S8.

Statistical Analysis of Global pH-Dependent Dissolution and Redeposition

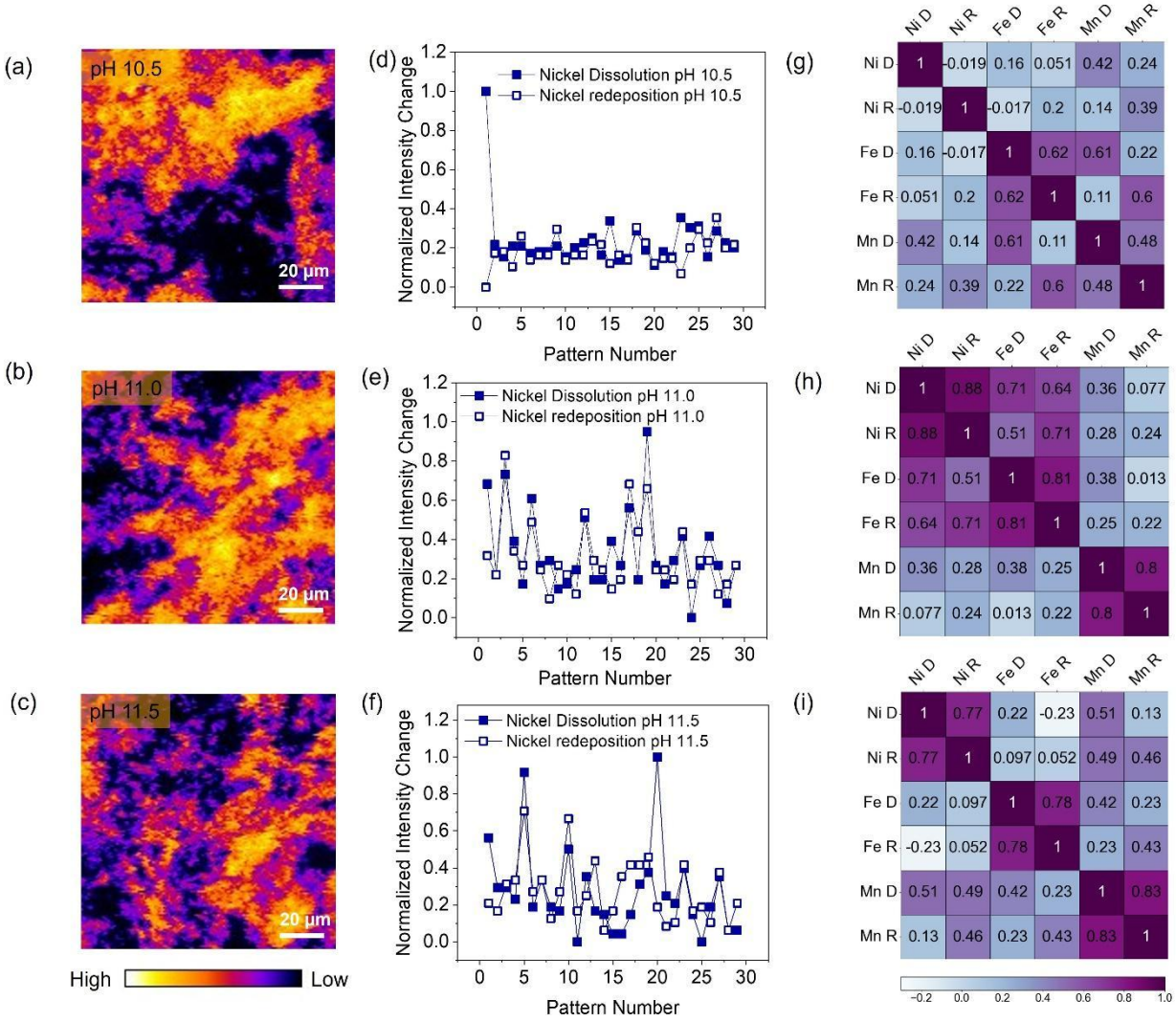

Figure 2: Relative D/R behavior of Ni, Fe and Mn as a function of pH and their correlation. (a-c) In-situ XFM mapping of the samples ($Ni_{1/3}Fe_{1/3}Mn_{1/3}(OH)_{2+x}$ deposited on carbon paper) acquired during a 13 min scan while immersed in NH_4OH solution of (a) pH 10.5 (b) pH 11.0 and (c) pH 11.5. These images correspond to the first Ni map in the time series and represent fluorescence intensity averaged over a 13-minute acquisition period. The images are composed of 140×140 pixels, with each pixel corresponding to 1 µm area on the sample. Net fluorescence intensity change for these datasets are shown in Figure S9. (d-f) Net dissolution and redeposition trends for Ni as a function of time are shown at (d) pH 10.5 (e) pH 11.0 and (f) pH 11.5. The corresponding data for Fe and Mn are provided in the supplementary document (Figure S10). Each pattern represents a differential image generated by subtracting two consecutive raw XFM scans taken ~13 minutes apart; thus, the x-axis reflects image-subtraction time points, not raw scan numbers. (g-i) Heatmaps showing the Pearson correlation among the Ni, Fe and Mn dissolution and

redeposition datasets are presented for (g) pH 10.5 (h) pH 11.0 and (i) pH 11.5. Image classification into 'dissolution' and 'redeposition' components and Pearson correlation calculation details are presented in the supplementary document (Figure S8, Note S1).

Dissolution and redeposition (D/R) behaviors in multicomponent systems are strongly influenced by chemical environment, particularly pH. To probe these effects, we calculated Pearson correlation analysis on time-resolved XFM data for Ni, Fe, and Mn to evaluate how D/R processes are temporally related within and across metal species. Clarifying these metal-metal correlations is key to understanding the reactivity and stability of systems such as electrocatalysts and battery electrodes.

Among the three transition metals, Ni exhibits the strongest pH-dependent change. At pH 10.5, it exhibits early rapid dissolution with very limited redeposition throughout the dataset (Figure 2d). As the pH rises, the system becomes more dynamic, with dissolution and redeposition occurring in more tightly coupled cycles (Figure 2e-2f). Fe and Mn follow a different trajectory. Even at pH 10.5 their dissolution and redeposition patterns rise and fall together (Figure S10a-10b). As pH increases, Fe and Mn D/R behavior remain highly synchronous (Figure S11-12). To quantify the dynamic relationships between dissolution and redeposition of Ni, Fe, and Mn across varying pH conditions, we computed Pearson correlation coefficients (r) for each pair of species-specific processes (TM D/R) at three different pH values 10.5, 11.0, and 11.5. The results are presented as heatmaps in Figure 2(g–i), with corresponding p-values listed in Table S2 – S4 and calculation details provided in Supplementary Note S1.

At pH 10.5, Ni dissolution and redeposition were essentially uncorrelated (r = –0.019), indicating that dissolution did not lead to immediate redeposition (Figure 2g). However, as the pH increased to 11.0 and 11.5, the correlation between Ni D and Ni R rose sharply to r = 0.88 and 0.77 respectively (Figure 2h-2i). This trend suggests a pH-dependent shift from decoupled to increasingly coupled D/R behavior for Ni. This can be attributed to both thermodynamic and kinetic factors. The K_{sp} value of $Ni(OH)_2$ is 5.48×10^{-16},[17] indicating it is sparingly soluble under neutral conditions. At higher pH, the elevated OH^- concentration shifts the dissolution equilibrium $Ni(OH)_2\,(s) \rightleftharpoons Ni^{2+}\,(aq) + 2OH^-\,(aq)$ toward the solid phase (common ion effect), further reducing

Ni^{2+} solubility. This suppression promotes local supersaturation and subsequent redeposition once dissolution occurs.[18] Moreover, Ni^{2+} forms highly stable ammonia complexes (log $K_6 \approx 9.08$),[19] which stabilize the dissolved Ni. But at higher pH local supersaturation can exceed the solubility threshold which can lead to rapid redeposition of Ni.

Fe exists in the Fe^{3+} oxidation state in the starting material (Figure S3-S4), and its D/R dynamics remained consistently correlated across the pH range, as can be seen in Figure 2g-2i ($r = 0.62$ at pH 10.5, rising to $r = 0.81$ at pH 11.0, and slightly decreasing to $r = 0.78$ at pH 11.5, with all p-values < 0.001). This persistent coupling implies a local feedback loop possibly facilitated by Fe^{3+}'s extremely low solubility (K_{sp} of $Fe(OH)_3 = 2.79 \times 10^{-39}$)[17] and weak ammonia complexation.[19] The very low solubility can lead to minor local fluctuations in Fe^{3+} concentration, which can then drive rapid redeposition in the high pH conditions. While Fe^{3+} is thermodynamically unstable in aqueous ammonia,[19] it may form insoluble oxyhydroxides rapidly, leading to redeposition.[20–22] Mn also showed increasing D/R coupling with pH ($r = 0.48$ at pH 10.5, 0.80 at pH 11.0 and 0.83 at pH 11.5, Figure 2g-2i), suggesting a similar transition to pH-driven local saturation and redeposition as seen with Ni. Mn^{2+} forms relatively weak complexes with ammonia (log $K_6 \approx 1.7$).[17,23] This provides some stabilization in solution but it is not strong enough to prevent redeposition. Localized redeposition may still occur under alkaline conditions, particularly in the presence of Mn^{3+}, which is known to undergo redox transitions that could influence surface reactivity.

In terms of cross-element correlation and interaction effects, at pH 10.5, Fe and Mn dissolution were strongly correlated ($r = 0.61$, Figure 2g), while Ni appeared largely decoupled from both. This suggests that Fe and Mn may undergo concurrent dissolution under lower pH conditions. At pH 11.0, a notable correlation emerged between Ni and Fe dissolution ($r = 0.71$, Figure 2h), indicative of increased kinetic coupling. This interaction diminished at pH 11.5, where Ni and Fe became largely decoupled, rather a new correlation was observed between Ni and Mn dissolution ($r = 0.51$, Figure 2i). The progression from Fe–Mn coupling at lower pH to Ni–Fe at intermediate pH, and Ni–Mn at higher pH suggests a pH-dependent shift in dominant dissolution interactions. This can be possibly due to divergence in solubility equilibria and the relative stability of metal–ammonia complexes under increasingly alkaline conditions. To build on this

understanding, we next examine how reaction rates of the transition metals evolve over time and how the system approaches spatial equilibrium as a function of pH, using cumulative intensity trends and probability density functions as quantitative descriptors of D/R behavior.

Reaction Rates and Spatial Equilibration across pH Conditions

To complement our correlation analysis and uncover how D/R processes evolve toward equilibrium, we next evaluated the relative reaction rates and spatial equilibration behavior of Ni, Fe, and Mn across different pH conditions. This analysis revealed that each metal responds uniquely to changes in alkalinity. Peak activity occurs at different pH values for each metal, and the spatial spread of reaction events becomes progressively more uniform at higher pH, indicating a convergence toward equilibrium.

From the cumulative sums of the D/R datasets across different pH values, we estimated the relative reaction rates of D and R events for the three metals using a linear regression method (Figure S13). The calculation details are given in supplementary Note S2. The estimated relative reaction rates for Ni, Fe and Mn D/R at different pH values are given in Table 1. These rates do not represent absolute chemical reaction rates but rather reflect the relative speed of net D/R activity as observed through in-situ fluorescence imaging. The slopes of cumulative intensity changes serve as a proxy for how quickly the system undergoes transformation under each condition.

Table 1. Estimation of relative reaction rates for TM D/R derived from the slopes of linear regression curves fitted to the cumulative sum of the D/R datasets:

	Relative Reaction Rates (a.u./min)					
pH	Ni D	Ni R	Fe D	Fe R	Mn D	Mn R
10.5	0.019	0.018	0.032	0.025	0.026	0.019
11.0	0.025	0.024	0.023	0.021	0.025	0.023
11.5	0.022	0.023	0.029	0.028	0.030	0.029

Table 1 highlights two clear trends: i) Each metal reaches its maximal overall D/R activity at a different pH: Ni at 11.0, Fe at 10.5, and Mn at 11.5 and ii) Although redeposition is typically slower than dissolution, the D and R rate gap diminishes as pH rises, implying that stronger alkalinity brings the system progressively closer to chemical equilibrium.

Because XFM offers high spatial resolution, it not only enables relative kinetic analysis but also allows us to resolve how D/R events evolve across localized regions, making it possible to investigate spatial equilibration processes as a function of pH. Among the three transition metals, Ni showed the highest sensitivity to pH, making it an illustrative case for demonstrating how pH influences the progression from localized to equilibrated interfacial reactions. We used probability density functions (PDFs) to quantify how Ni D/R events relate to the initial material distribution captured in raw fluorescence images.

First, the initial raw fluorescence image at the first time point was divided into 50 equally spaced intensity bins (illustrated in Figure S14). This image represents the baseline distribution of Ni, across the carbon paper surface, and the bins served as proxies for local metal concentration. Then we quantified the number of dissolution and redeposition events occurring at each bin across all time points. This allowed us to calculate the empirical probability distribution of dissolution and redeposition as a function of initial local metal concentration (raw intensity), allowing us to quantify how event likelihood varies across the concentration spectrum. We then applied kernel density estimation (KDE) to these probability distributions to generate smooth and continuous probability density functions (Figure 3). To minimize the influence of background signal, low-intensity bins below a defined threshold were excluded from the analysis. Skewness was computed from the KDE curves at each time point to quantify asymmetry in the spatial distribution of D/R activity relative to the initial metal intensity (Figure S15). Temporal changes in skewness were

interpreted as the system's progression toward spatial equilibrium. Strong skewness indicates localized, non-equilibrated behavior, while near-zero and stable values suggest more symmetric, delocalized, and equilibrated reaction patterns. [24,25]

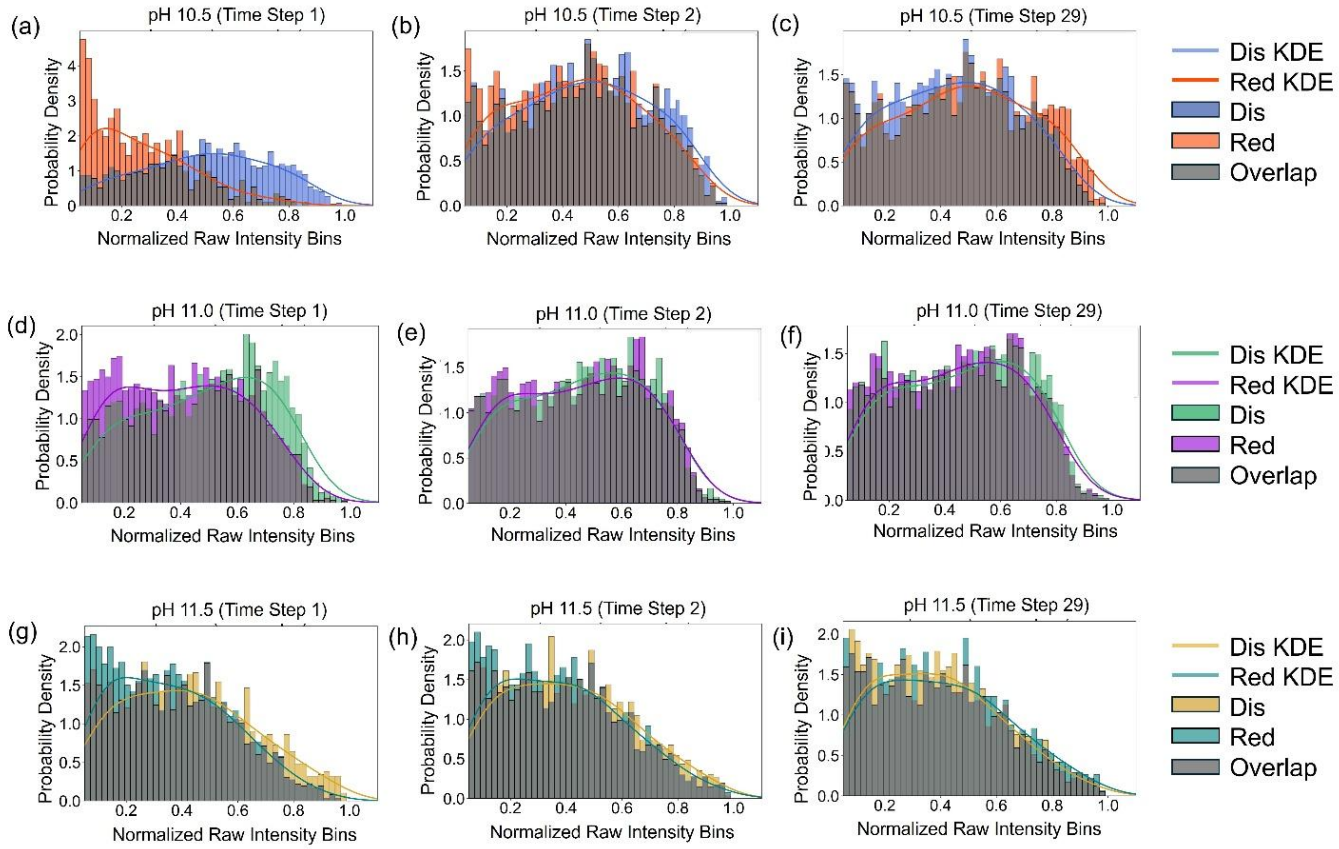

Figure 3: Stabilization of Ni D/R equilibrium under varying pH conditions, visualized through histogram-based probability distributions with overlaid kernel density estimates (KDEs). Each panel shows the probability distribution of D/R events as a function of initial material distribution, captured via normalized raw fluorescence intensity from X-ray fluorescence microscopy (XFM) images of Ni. The x-axis represents 50 equally spaced intensity bins from the first (baseline) fluorescence image, serving as proxies for the local metal concentration across the substrate. The y-axis indicates probability density of D/R events occurring within each bin. Bars represent marginalized probability densities: dissolution (Dis) and redeposition (Red) histograms are overlaid, with intersecting regions shaded in gray to highlight spatial overlap in activity. Colored curves show KDEs applied to the binned probability distributions, serving as smoothed approximations of the histogram shapes. Panels (a–c) correspond to pH 10.5 at time points 1, 2, and 29; (d–f) to pH 11.0; and (g–i) to pH 11.5.

Figure 3 shows the evolution of Ni dissolution and redeposition distributions at three representative time points (1st, 2nd, and 29th) under each pH condition, with full time series available in Supplementary Movies A1–A3. The corresponding KDE skewness values for all time points are summarized in Supplementary Figure S15.

At pH 10.5, the skewness values for dissolution and redeposition demonstrate an evident difference (Figure 3a and S14), reflecting spatial separation between the two processes at early stages. Dissolution occurs mostly in high-intensity regions, while redeposition remains skewed toward lower intensities. This asymmetry persists through the initial scans, with gradual convergence observed over time (Figure S15). The slow reduction in the skewness difference and the mild fluctuations across time steps indicate a delayed approach to spatial equilibration, where D/R activity remains partially localized for an extended period before becoming more uniformly distributed.

At pH 11.0, the skewness values for dissolution and redeposition diverge at the first time point (Figure 3d), less sharply than at pH 10.5 (Figure 3a), indicating spatially localized and asymmetric D/R activity. However, by the second time point (Figure 3e), this gap narrows sharply, signaling a rapid onset of equilibration. Despite this early convergence, the skewness values continue to fluctuate throughout the time series (Figure S15), suggesting that D/R events remain spatially dynamic. This behavior reflects a fast but spatially unstable equilibration process, where reactions quickly delocalize but continue to reorganize locally.

At pH 11.5, dissolution and redeposition begin with nearly overlapping skewness values that remain close to zero and stable over time (Figure 3g-3i and S14). This consistent symmetry indicates that spatial equilibration is achieved almost immediately and maintained throughout the experiment. The lack of significant skewness shifts or fluctuations points to a fast and spatially stable equilibration process, where D/R activity is uniformly distributed from the outset.

These observations collectively show that higher pH accelerates both the kinetics and the spatial delocalization of D/R processes. At lower pH, reactions are localized and spatially asymmetric, while at higher pH, they occur more uniformly across the material surface. In the following section, we build on this understanding using statistical tools to further quantify these evolving spatial patterns.

Statistical Characterization of Spatial Patterns of the Dissolved and Redeposited Species

In addition to analyzing the chemical and spatial kinetics of metal dissolution and redeposition (D/R) as a function of pH, we investigated the nature of spatial distribution of the D/R species. Subtle shifts in local texture, often imperceptible in raw intensity maps, can reveal underlying reaction heterogeneity and interfacial instability. In this section, we adopt a statistical approach to quantify the spatial heterogeneity patterns and monitor the changes of these patterns over time. We find that spatial heterogeneity is highest when D/R processes are decoupled and become increasingly suppressed as pH promotes tighter chemical and spatial coupling.

Figure S16 presents the raw XFM map of Ni at pH 10.5, alongside a time series of images highlighting regions of positive (redeposition) and negative (dissolution) intensity changes at selected time points. In these images, dissolution appears to be initiated from high-intensity clustered regions, which gradually diminish and become more diffuse over time. In contrast, redeposition features are sparse from the outset. Both datasets reveal subtle but distinct spatial changes in the distribution of D/R species over time. These observations prompted a key question: can these subtle spatial changes be quantified to track how D/R behavior evolves across different metals and pH conditions? Such spatial characterizations are critical for understanding the degree of heterogeneity in D/R reactions and their dependence on the type of transition metal and pH.

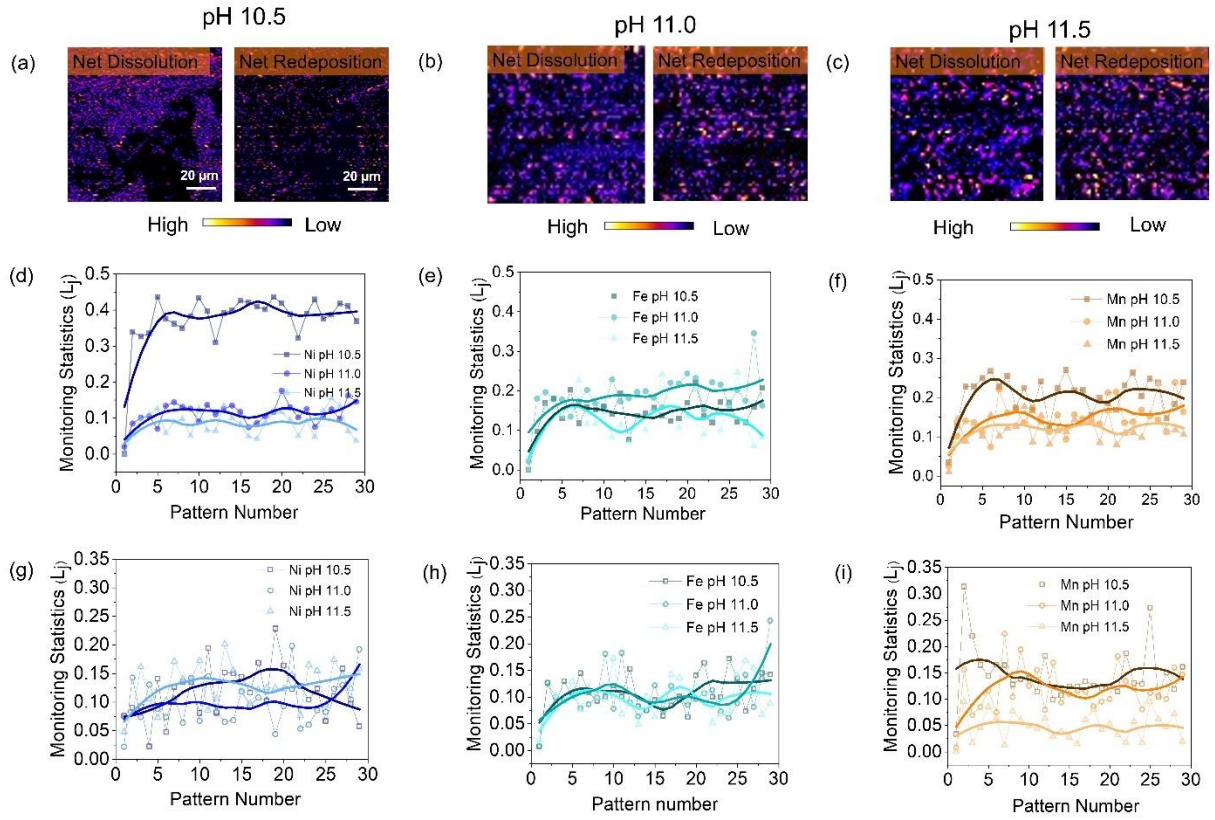

Figure 4: Spatial analysis of Ni, Fe, and Mn dissolution and redeposition (D/R) behavior under varying pH conditions. In situ XFM maps show net Ni D/R at the first time point (t ≈ 13 min) for (a) pH 10.5, (b) pH 11.0, and (c) pH 11.5. Monitoring statistics quantify global spatial pattern changes in dissolution datasets for (d) Ni, (e) Fe, and (f) Mn, and in redeposition datasets for (g) Ni, (h) Fe, and (i) Mn, across time (indicated by pattern number, each pattern represents a differential image generated by subtracting two consecutive raw XFM scans taken ~13 minutes apart; thus, the x-axis reflects image-subtraction time points, not raw scan numbers.) and pH. Higher values reflect greater deviation from the initial spatial configuration, indicating stronger textural evolution. LOESS-smoothed lines are overlaid on each dataset to highlight temporal trends and pH-dependent behavior.

To quantify temporal changes in the spatial distribution of D/R events, we employed a monitoring statistics framework based on stochastic textured surface (STS) analysis.[26] In our system, the dissolution and redeposition events generate subtle and evolving patterns that do not conform to well-defined shapes or features. This makes conventional image processing techniques ineffective or unreliable. Instead, the STS framework treats the image as a realization of a stochastic process, where each pixel's intensity value depends only on the intensities of its spatial

neighbors. By applying a regression-tree algorithm to capture these local dependencies, we established a statistical model of the baseline texture using the first image in the dataset (in-control image). Subsequent images are compared to this baseline using a likelihood-ratio-based monitoring statistic, L_j, which quantifies the degree of deviation in overall image texture. A one-pixel neighborhood was selected to balance sensitivity and model stability, and neighborhoods were defined in a consistent left-to-right, top-to-bottom scan. A higher L_j value reflects a larger deviation from the original spatial pattern, which may arise from increasing spatial heterogeneity in the D/R distribution. This approach captures gradual and system-wide changes in spatial patterns that would have been missed by conventional feature-based methods. Full details of the L_j computation are provided in Supplementary Note S4.

The monitoring statistic values for Ni, Fe, and Mn dissolution across different pH values are shown in Figures 4(d–f), with the corresponding redeposition datasets presented in Figures 4(g–i). A smoothing line using locally estimated scatterplot smoothing (LOESS) is overlaid on each dataset to highlight temporal trends and pH-dependent behavior (see Note S5).[27,28] Among the three metals, nickel exhibits the most pronounced pH-dependent shift in L_j. At pH 10.5, Ni dissolution yields high L_j values (Figure 4d), while Ni redeposition shows low L_j values (Figure 4g). This asymmetry arises from the decoupled nature of Ni dissolution and redeposition at this pH, as evidenced by their near-zero correlation ($r = –0.019$, Figure 2g) and delayed spatial stabilization seen in the PDF analysis (Figure 3a). The elevated L_j values indicate that Ni dissolution causes notable deviations in image texture, suggesting greater change in spatial heterogeneity, whereas redeposition events are sparse and demonstrate less variations in spatial pattern. In contrast, at pH 11.0 and 11.5, where Ni shows strong D/R coupling ($r = 0.88$ and 0.77, respectively, see Figure 2h-2i) and nearly matched reaction rates (see Table 1), L_j values remain low for both processes. This suggests that dissolution and redeposition occur in a more spatially synchronized and balanced manner, with minimal net disruption to the substrate texture. This is consistent with the PDF skewness stabilizing rapidly at higher pH values (Figure 3 and Figure S15), reflecting a well-equilibrated spatial distribution of events. These results show that decoupled or asynchronous D/R behavior (particularly dominated by the dissolution process) can lead to greater spatial heterogeneity, whereas tightly coupled processes promote more uniform spatial distributions.

Fe shows consistently moderate L_j values across all pH levels, with dissolution L_j fluctuating around 0.14 to 0.19 (Figure 4e) and redeposition L_j fluctuating around 0.10 (Figure 4h). These stable yet slightly fluctuating monitoring statistics indicate ongoing but spatially limited textural fluctuations. This behavior can redeposit be explained by iron's strong D/R coupling across all pH (Figure 2g-i) and its inherently low solubility ($K_{sp} \sim 10^{-39}$), which may cause Fe^{3+} to almost immediately upon dissolution. Moreover, the weak complexation of Fe^{3+} with ammonia may limit its diffusion, resulting in minimal spatial reorganization even if the interface remains chemically active. Among the three metals Mn displays the most irregular L_j trends, particularly in the dissolution datasets, where values decrease from 0.20 ± 0.05 at pH 10.5 to 0.15 ± 0.05 at pH 11.0 and 0.12 ± 0.05 at pH 11.5 (Figure 4f). Redeposition L_j values also decline substantially with increasing pH (from 0.15 ± 0.05 at pH 10.5 to 0.05 ± 0.03 at pH 11.5, Figure 4i). These progressively decreasing L_j values for both dissolution and redeposition indicate that the spatial texture of the system changes less over time, suggesting that D/R events are occurring in a more spatially and temporally aligned manner at higher pH. This is also supported by the increasing D/R correlation for Mn, which rises from 0.48 to 0.83 across the pH range (Figure 2 g-i). The initially erratic spatial evolution at lower pH may result from redox cycling between Mn^{2+} and Mn^{3+}, which can introduce local fluctuations in solubility and reactivity. Overall, these findings highlight that monitoring statistics can serve as a sensitive metric for quantifying the dynamics of spatial heterogeneity and localization in dynamic interfacial processes.

Modulating the Interfacial Reaction Kinetics:

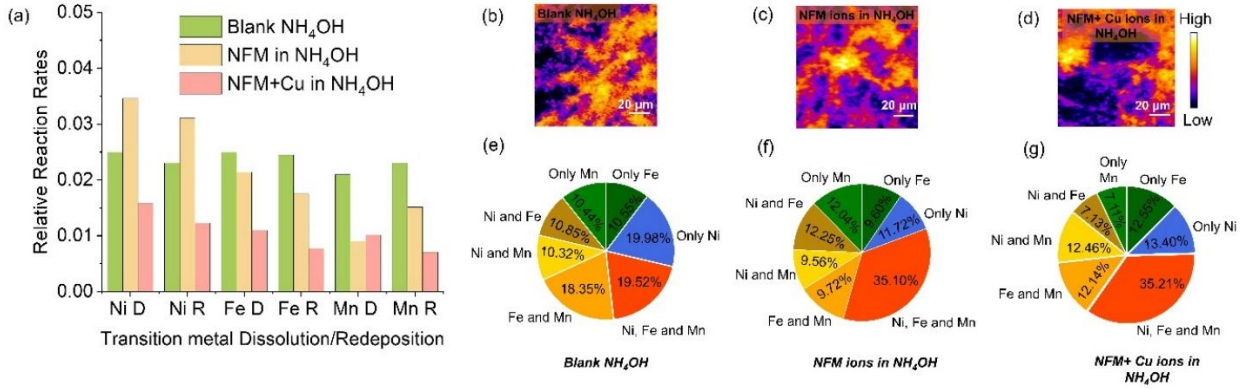

Figure 5: Manipulating the D/R behavior of Ni, Fe and Mn by modulating the solvent environment with additional ions. (a) Estimation of reaction rates from the slopes of cumulative sums of the Ni, Fe and Mn D/R datasets in blank NH_4OH, NH_4OH with NFM ions and NH_4OH with NFM+Cu ions. (b-d) in-situ XFM mapping of Ni in samples containing pre-deposited $Ni_{1/3}Fe_{1/3}Mn_{1/3}(OH)_{2+x}$ particles on the substrate, after immersion in three different electrolytes: (b) blank NH_4OH (c) NH_4OH with Ni^{2+}, Fe^{3+} and Mn^{2+} ions (NFM ions), (d) NH_4OH with Ni^{2+}, Fe^{3+}, Mn^{2+} and Cu^{2+} ions (NFM+Cu ions). (e-g) Analysis of the elemental overlap in the redeposition datasets in (e) blank NH_4OH (f) NH_4OH with NFM ions, (g) NH_4OH with NFM+Cu ions. The pie charts illustrate the distribution of pixels within the datasets where the elements exhibit single-element redeposition, two-element redeposition, or three-element redeposition.

Having established the spatial and temporal characteristics of the D/R behavior and texture-based spatial statistics, we next investigated whether the interfacial reaction kinetics could be intentionally modulated by altering the solvent environment. For this purpose, we performed electrolyte modification experiments at pH 11.0 by introducing 10 µL of 10 mM Ni^{2+}, Fe^{3+}, and Mn^{2+} ions directly into the system. This led to a notable increase in the reaction rates for Ni (Figure 5a and Table S5), with the relative rate of dissolution increasing from 0.025 a.u./min to 0.034 a.u./min, and redeposition from 0.024 a.u./min to 0.031 a.u./min. However, for Fe and Mn the effect was either marginal or slightly suppressive, suggesting that the kinetic response to local ion enrichment is metal-specific. To examine whether the reaction kinetics could also be selectively suppressed, we conducted a parallel experiment in which Cu^{2+} was added along with Ni^{2+}, Fe^{3+}, and Mn^{2+}. Copper was chosen due to its significantly higher affinity for ammonia relative to the native metal ions,[19] which was expected to reduce the availability of free NH_3 ligands required for

metal–ligand complexation. Upon Cu^{2+} addition, we observed a pronounced suppression of both dissolution and redeposition rates across all metals, supporting the hypothesis that competing complexation can effectively inhibit reaction dynamics. Net fluorescence intensity changes for the raw, dissolution, and redeposition datasets from both experiments are presented in Figures S16–S18. Estimated relative reaction rates from the linear regression of the cumulative sums for both experiments are shown in Figure S20 and listed in Table S5. To understand whether these rate changes were accompanied by shifts in spatial metal distribution, we conducted a pixel-wise XFM analysis quantifying how many pixels contained signals from individual metals versus overlapping combinations. In the control condition (blank NH_4OH, no ions added), only 19.5% of the redeposition pixels showed co-localized Ni, Fe, and Mn signals. This analysis was restricted to the redeposition datasets, which represent only the newly redeposited material during the experiment and exclude the pre-existing $Ni_{1/3}Fe_{1/3}Mn_{1/3}(OH)_{2+x}$ particles through image subtraction. This fraction rose to over 35% in both ion doped conditions, indicating a dramatic increase in regions where all three metals are simultaneously active (Figure 5e-g and Figure S21). This enhanced co-localization suggests that added ions promote local supersaturation and more synchronized redeposition behaviors among different transition metals. For Ni, this also translated to faster dynamic changes, as reflected by increased D/R signal rates. In contrast, Cu^{2+} addition likely disrupts this cooperative effect by outcompeting Ni^{2+}, Fe^{3+}, and Mn^{2+} for ammonia ligands, thereby suppressing metal-ion mobility and interfacial exchange. These findings demonstrate that interfacial D/R kinetics can be selectively modulated through ion-specific electrolyte modifications, either by tuning the local supersaturation of reactive species or introducing strongly chelating foreign ions. Such control strategies are directly relevant to optimizing materials synthesis in alkaline environments, where particle morphology, composition, and homogeneity are strongly influenced by dissolution and redeposition dynamics. While beam stability is an important consideration in extended XFM measurements, the metal-specific, pH-dependent, and ion-sensitive trends observed here cannot arise from uniform beam-induced attenuation and therefore reflect genuine interfacial D/R processes rather than measurement artifacts.

Conclusion

Capturing the dynamic interplay between dissolution and redeposition (D/R) processes at reactive interfaces remains a significant challenge, particularly in chemically complex systems where spatial heterogeneity and elemental interdependencies obscure mechanistic insights. In this study, we employed in situ synchrotron-based X-ray fluorescence microscopy (XFM) to systematically investigate the D/R kinetics of Ni, Fe, and Mn from a model $Ni_{1/3}Fe_{1/3}Mn_{1/3}(OH)_{2+x}$ material under controlled alkaline environments. Although our instrumental parameters match the spatial resolution, sensitivity, and acquisition speed of state-of-the-art operando XFM studies (see Table S6), the advance of this work lies not in improved microscope performance but in the analytical methodology required to extract information from systems exhibiting extremely subtle near-equilibrium interfacial dynamics. Our statistical and spatial analysis framework provides insight into dissolution/redeposition processes that are not visually discernible and would be missed by conventional electrochemical XFM analysis protocols available in literature. Our approach integrates high-resolution elemental imaging with spatial statistics and reaction rate estimation to disentangle the complex behaviors governing multielement D/R processes. Specifically, our work highlights the following key insights:

i) Nickel exhibited a strong transition from decoupled to tightly coupled D/R cycles with increasing pH, attributed to changes in solubility and complexation equilibria. Iron displayed consistent D/R coupling across all pH values due to its extremely low solubility and rapid redeposition behavior, while manganese showed progressively stronger D/R correlation with increasing pH, possibly due to redox cycling and weaker complexation.

ii) Each metal reaches its maximum overall D/R activity at a different pH, highlighting distinct pH sensitivities for each metal. Although dissolution generally outpaced redeposition, this gap narrowed as the pH increased, indicating that stronger alkalinity enhances the system's approach toward local equilibrium.

iii) At higher pH, the spatial patterns of D/R events became more uniform and delocalized, stabilizing more rapidly over time. Stronger alkalinity not only accelerates reaction rates but also promotes spatial equilibration across the surface. Spatial heterogeneity was greatest when dissolution and redeposition occurred out of sync, particularly at low pH, whereas tightly coupled processes at higher pH maintained more uniform substrate textures.

iv) Interfacial D/R kinetics can be actively tuned by modifying the electrolyte composition. While Ni^{2+}, Fe^{3+}, and Mn^{2+} additions enhanced local supersaturation and reaction rates for Ni, Cu^{2+} suppressed kinetics across all metals due to competitive complexation with ammonia.

Altogether, this study provides a unified framework to understand, quantify, and manipulate transition metal D/R behavior in alkaline media. Our image-based and statistically-guided methodology offers a robust framework for probing complex interfacial dynamics across a wide range of materials systems, with direct relevance to technologies such as battery electrodes, electrocatalysts, materials synthesis, and metal recovery processes. This framework also provides a modular foundation that can be readily adapted for true operando environments by incorporating system-specific experimental controls. For instance, the setup could be expanded by integrating a three-electrode configuration to apply controlled potentials, introducing flow-through channels to regulate mass transport, implementing temperature-controlled cell bodies to tune reaction kinetics, or coupling XFM with concurrent spectroscopies (XAS/XRD) under bias to simultaneously track structural and compositional changes. In parallel, the data-analysis platform developed here (based on pixel-wise D/R separation, statistical correlation mapping, probability-distribution analysis, and texture-based monitoring statistics) is entirely generalizable and can be applied to any multi-element operando XFM dataset to extract hidden kinetic and spatial information that conventional image-based approaches would overlook. These insights not only deepen our mechanistic understanding but also provide actionable strategies for designing materials and electrolytes to achieve targeted performance in practical energy and environmental applications.

Supporting Information

Additional characterization, in-situ XFM datasets, data-analysis workflows, reaction-rate calculations, spatial statistics, and tabulated results.

Acknowledgements

The work was supported by the National Science Foundation under DMR 2325464. The use of the Stanford Synchrotron Radiation Lightsource, SLAC National Accelerator Laboratory, was supported by the U.S. Department of Energy, Office of Science, Office of Basic Energy Sciences under Contract no. DE-AC02-76SF00515. This research used resources of the beamline 5-ID at National Synchrotron Light Source II, a U.S. Department of Energy (DOE) Office of Science User

Facility operated for the DOE Office of Science by Brookhaven National Laboratory under Contract No. DE-SC0012704. This research used resources of the Advanced Photon Source; a U.S. Department of Energy (DOE) Office of Science User Facility operated for the DOE Office of Science by Argonne National Laboratory under Contract no. DE-AC02 06CH11357. This work used shared facilities at the Nanoscale Characterization and Fabrication Laboratory, which is funded and managed by Virginia Tech's Institute for Critical Technology and Applied Science. Additional support is provided by the Virginia Tech National Center for Earth and Environmental Nanotechnology Infrastructure (NanoEarth), a member of the National Nanotechnology Coordinated Infrastructure (NNCI), supported by NSF (ECCS 1542100 and ECCS 2025151). F.L. acknowledges the NCFL Faculty Fellowship program. This project was partially supported by the Virginia Tech College of Science Academy of Data Science Discovery Fund (Fund Number: 120691).

Conflict of Interest

The authors declare the following competing financial interest(s): Dr. Feng Lin is a co-founder of Fermi Energy Inc., which develops and commercializes battery materials. Dr. Feng Lin is a non-paid adjunct faculty member at Virginia Tech.

Data Availability

Data is available upon request.

References:

(1) Guidetti, G.; Zanini, R.; Franceschin, G.; Moglianetti, M.; Kim, T.; Cohan, N.; Chan, L.; Treadgold, J.; Traviglia, A.; Omenetto, F. G. Photonic Crystals Built by Time in Ancient Roman Glass. *Proceedings of the National Academy of Sciences* **2023**, *120* (39). https://doi.org/10.1073/pnas.2311583120.

(2) Sievers, C.; Noda, Y.; Qi, L.; Albuquerque, E. M.; Rioux, R. M.; Scott, S. L. Phenomena Affecting Catalytic Reactions at Solid–Liquid Interfaces. *ACS Catal* **2016**, *6* (12), 8286–8307. https://doi.org/10.1021/acscatal.6b02532.

(3) Kuai, C.; Xu, Z.; Xi, C.; Hu, A.; Yang, Z.; Zhang, Y.; Sun, C.-J.; Li, L.; Sokaras, D.; Dong, C.; Qiao, S.-Z.; Du, X.-W.; Lin, F. Phase Segregation Reversibility in Mixed-Metal Hydroxide Water Oxidation Catalysts. *Nat Catal* **2020**, *3* (9), 743–753. https://doi.org/10.1038/s41929-020-0496-z.

(4) Popovic, S.; Bele, M.; Hodnik, N. Reconstruction of Copper Nanoparticles at Electrochemical CO_2 Reduction Reaction Conditions Occurs *via* Two-step Dissolution/Redeposition Mechanism. *ChemElectroChem* **2021**, *8* (14), 2634–2639. https://doi.org/10.1002/celc.202100387.

(5) Popović, S.; Smiljanić, M.; Jovanovič, P.; Vavra, J.; Buonsanti, R.; Hodnik, N. Stability and Degradation Mechanisms of Copper-Based Catalysts for Electrochemical CO_2 Reduction. *Angewandte Chemie* **2020**, *132* (35), 14844–14854. https://doi.org/10.1002/ange.202000617.
(6) Speck, F. D.; Zagalskaya, A.; Alexandrov, V.; Cherevko, S. Periodicity in the Electrochemical Dissolution of Transition Metals. *Angewandte Chemie International Edition* **2021**, *60* (24), 13343–13349. https://doi.org/10.1002/anie.202100337.
(7) Lakhan, M. N.; Hanan, A.; Hussain, A.; Ali Soomro, I.; Wang, Y.; Ahmed, M.; Aftab, U.; Sun, H.; Arandiyan, H. Transition Metal-Based Electrocatalysts for Alkaline Overall Water Splitting: Advancements, Challenges, and Perspectives. *Chemical Communications* **2024**, *60* (39), 5104–5135. https://doi.org/10.1039/D3CC06015B.
(8) Wu, D.; King, S. T.; Sadique, N.; Ma, L.; Ehrlich, S. N.; Ghose, S.; Bai, J.; Zhong, H.; Yan, S.; Bock, D. C.; Takeuchi, E. S.; Marschilok, A. C.; Housel, L. M.; Wang, L.; Takeuchi, K. J. *Operando* Investigation of Aqueous Zinc Manganese Oxide Batteries: Multi-Stage Reaction Mechanism Revealed. *J Mater Chem A Mater* **2023**, *11* (30), 16279–16292. https://doi.org/10.1039/D3TA01549A.
(9) Becknell, N.; Lopes, P. P.; Hatsukade, T.; Zhou, X.; Liu, Y.; Fisher, B.; Chung, D. Y.; Kanatzidis, M. G.; Markovic, N. M.; Tepavcevic, S.; Stamenkovic, V. R. Employing the Dynamics of the Electrochemical Interface in Aqueous Zinc-Ion Battery Cathodes. *Adv Funct Mater* **2021**, *31* (35). https://doi.org/10.1002/adfm.202102135.
(10) Paudel, N.; Ale Magar, B.; Acharya, K.; Lambert, T. N.; Vasiliev, I. Influence of Defects and Surfaces on the Electrochemical Performance of MnO_2 Cathodes in Rechargeable Alkaline Zn/MnO_2 Batteries: A First-Principles Study. *ACS Appl Energy Mater* **2024**, *7* (7), 2767–2778. https://doi.org/10.1021/acsaem.3c03200.
(11) Wu, D.; King, S. T.; Sadique, N.; Ma, L.; Ehrlich, S. N.; Ghose, S.; Bai, J.; Zhong, H.; Yan, S.; Bock, D. C.; Takeuchi, E. S.; Marschilok, A. C.; Housel, L. M.; Wang, L.; Takeuchi, K. J. *Operando* Investigation of Aqueous Zinc Manganese Oxide Batteries: Multi-Stage Reaction Mechanism Revealed. *J Mater Chem A Mater* **2023**, *11* (30), 16279–16292. https://doi.org/10.1039/D3TA01549A.
(12) Zhang, Y.; Hu, A.; Xia, D.; Hwang, S.; Sainio, S.; Nordlund, D.; Michel, F. M.; Moore, R. B.; Li, L.; Lin, F. Operando Characterization and Regulation of Metal Dissolution and Redeposition Dynamics near Battery Electrode Surface. *Nat Nanotechnol* **2023**, *18* (7), 790–797. https://doi.org/10.1038/s41565-023-01367-6.
(13) Kuai, C.; Liu, L.; Hu, A.; Zhang, Y.; Zhang, Y.; Xia, D.; Nordlund, D.; Sokaras, D.; Decarolis, D.; Gianolio, D.; Xin, H.; Li, L.; Lin, F. Dissolved Fe Species Enable a Cooperative Solid–Molecular Mechanism for the Oxygen Evolution Reaction on NiFe-Based Catalysts. *Nat Catal* **2025**, *8* (6), 523–535. https://doi.org/10.1038/s41929-025-01342-5.
(14) Zhang, Y.; Hu, A.; Maxey, E.; Li, L.; Lin, F. Spatiotemporal Visualization and Chemical Identification of the Metal Diffusion Layer at the Electrochemical Interface. *J Electrochem Soc* **2022**, *169* (10), 100512. https://doi.org/10.1149/1945-7111/ac964b.
(15) Min, J.; Bak, S.-M.; Zhang, Y.; Yuan, M.; Pietra, N. F.; Russell, J. A.; Deng, Z.; Xia, D.; Tao, L.; Du, Y.; Xiong, H.; Li, L.; Madsen, L. A.; Lin, F. Investigating the Effect of Heterogeneities across the Electrode|multiphase Polymer Electrolyte Interfaces in High-Potential Lithium Batteries. *Nat Nanotechnol* **2025**, *20* (6), 787–797. https://doi.org/10.1038/s41565-025-01885-5.
(16) Nazaretski, E.; Coburn, D. S.; Xu, W.; Ma, J.; Xu, H.; Smith, R.; Huang, X.; Yang, Y.; Huang, L.; Idir, M.; Kiss, A.; Chu, Y. S. A New Kirkpatrick–Baez-Based Scanning Microscope for the

Submicron Resolution X-Ray Spectroscopy (SRX) Beamline at NSLS-II. *J Synchrotron Radiat* **2022**, *29* (5), 1284–1291. https://doi.org/10.1107/S1600577522007056.
(17) John A Dean, *Lange's Handbook of Chemistry*, McGraw-Hill, 1999.
(18) Hall, D. S.; Lockwood, D. J.; Bock, C.; MacDougall, B. R. Nickel Hydroxides and Related Materials: A Review of Their Structures, Synthesis and Properties. *Proceedings of the Royal Society A: Mathematical, Physical and Engineering Sciences* **2015**, *471* (2174), 20140792. https://doi.org/10.1098/rspa.2014.0792.
(19) Smith, R. M. ; M. A. E. *Critical Stability Constants* ; Springer, 1989.
(20) Furcas, F. E.; Lothenbach, B.; Mundra, S.; Borca, C. N.; Albert, C. C.; Isgor, O. B.; Huthwelker, T.; Angst, U. M. Transformation of 2-Line Ferrihydrite to Goethite at Alkaline PH. *Environ Sci Technol* **2023**, *57* (42), 16097–16108. https://doi.org/10.1021/acs.est.3c05260.
(21) Furcas, F. E.; Mundra, S.; Lothenbach, B.; Angst, U. M. Speciation Controls the Kinetics of Iron Hydroxide Precipitation and Transformation at Alkaline PH. *Environ Sci Technol* **2024**, *58* (44), 19851–19860. https://doi.org/10.1021/acs.est.4c06818.
(22) Mahasti, N. N. N.; Shih, Y.-J.; Huang, Y.-H. Removal of Iron as Oxyhydroxide (FeOOH) from Aqueous Solution by Fluidized-Bed Homogeneous Crystallization. *J Taiwan Inst Chem Eng* **2019**, *96*, 496–502. https://doi.org/10.1016/j.jtice.2018.12.022.
(23) Lamb, J.; Manthiram, A. Synthesis Control of Layered Oxide Cathodes for Sodium-Ion Batteries: A Necessary Step Toward Practicality. *Chemistry of Materials* **2020**, *32* (19), 8431–8441. https://doi.org/10.1021/acs.chemmater.0c02435.
(24) Zhang, Y.; Hu, A.; Xia, D.; Hwang, S.; Sainio, S.; Nordlund, D.; Michel, F. M.; Moore, R. B.; Li, L.; Lin, F. Operando Characterization and Regulation of Metal Dissolution and Redeposition Dynamics near Battery Electrode Surface. *Nat Nanotechnol* **2023**, *18* (7), 790–797. https://doi.org/10.1038/s41565-023-01367-6.
(25) Hu, A.; Zhang, Y.; Yang, F.; Hwang, S.; Sainio, S.; Nordlund, D.; Maxey, E.; Dai, Q.; Gu, J.; Li, L.; Lin, F. Manipulating Interfacial Dissolution–Redeposition Dynamics to Resynthesize Electrode Surface Chemistry. *ACS Energy Lett* **2022**, *7* (8), 2588–2594. https://doi.org/10.1021/acsenergylett.2c01186.
(26) Bui, A. T.; Apley, D. W. Robust Monitoring of Stochastic Textured Surfaces. *Int J Prod Res* **2022**, *60* (16), 5071–5086. https://doi.org/10.1080/00207543.2021.1949642.
(27) Cleveland, W. S. Robust Locally Weighted Regression and Smoothing Scatterplots. *J Am Stat Assoc* **1979**, *74* (368), 829–836. https://doi.org/10.1080/01621459.1979.10481038.
(28) Cleveland, W. S.; Devlin, S. J. Locally Weighted Regression: An Approach to Regression Analysis by Local Fitting. *J Am Stat Assoc* **1988**, *83* (403), 596–610. https://doi.org/10.1080/01621459.1988.10478639.

ToC image

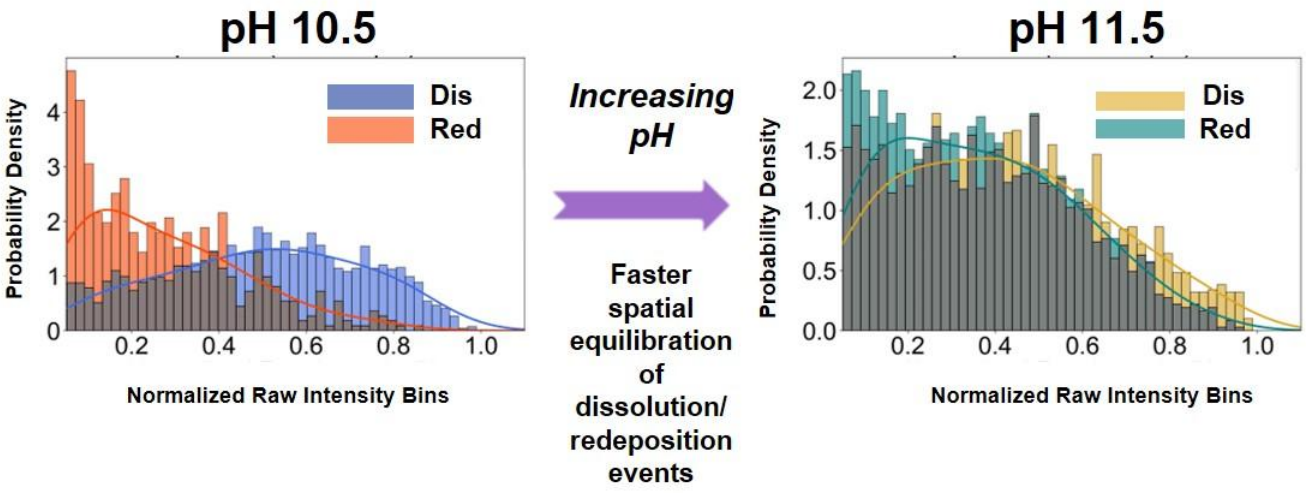
pH 10.5
Dis
Red
Probability Density
Normalized Raw Intensity Bins
Increasing pH
Faster spatial equilibration of dissolution/ redeposition events
pH 11.5
Dis
Red
Probability Density
Normalized Raw Intensity Bins